Monthly Notices of the ROYAL ASTRONOMICAL SOCIETY

MNRAS **548,** 1–15 (2026)
Advance Access publication 2026 March 19

https://doi.org/10.1093/mnras/stag545

The origin of extreme N-emitters in star-forming galaxies at $z < 0.5$ with DESI DR1

Souradeep Bhattacharya ★ and Chiaki Kobayashi

Centre for Astrophysics Research, Department of Physics, Astronomy and Mathematics, University of Hertfordshire, Hatfield AL10 9AB, UK

Accepted 2026 March 18. Received 2026 March 17; in original form 2025 August 16

ABSTRACT

Extreme nitrogen enhancement relative to oxygen, recently found in very high-redshift galaxies, has been seen in local star-forming galaxies (SFGs) displaying high log(N/O) values (≥ -1.1) at relatively low O abundances, $12 + \log(\mathrm{O/H}) \leq 8$. Understanding the physical origins of these extreme N-emitters at low redshifts enables us to constrain better chemical enrichment mechanisms that drove such high log(N/O) values in the early Universe. With direct N and O abundances derived for 944 SFGs with spectroscopic observational data from the Dark Energy Spectroscopic Instrument Data Release 1 (DESI DR1), we report the discovery of 19 extreme N-emitters at low z ($z < 0.5$). Our sample of N-emitters represents a fivefold increase in their known number at low z with $12 + \log(\mathrm{O/H}) \leq 8$, and statistically, 2.21 ± 0.91 per cent of DESI DR1 SFGs with reliable O and N abundances obtained directly are extreme N-emitters. The sample spans a mass range of $\sim 10^7$–10^{10} $\mathrm{M}_\odot$ with a $12 + \log(\mathrm{O/H})$ range of ∼7.1–8.2, and the N-emitter fraction is found to increase with increasing stellar mass and decreasing metallicity. The most extreme N-emitter in our sample has $\log(\mathrm{N/O}) = -0.53 \pm 0.13$, while also having the lowest, $12 + \log(\mathrm{O/H}) = 7.08 \pm 0.09$, and the highest stellar mass, $\log(M_*/\mathrm{M}_\odot) = 9.95 \pm 0.13$, among our sample. With galactic chemical evolution models, we show that sustained N-enhancement by asymptotic giant branch stars, in conjunction with the presence of outflows during the evolution of the galaxy, can well explain the high log(N/O) of low-z extreme N-emitters. While single starbursts with outflow are sufficient to explain lower mass N-emitters, more massive ones require a dual starburst scenario where a secondary starburst is triggered by the inflow of gas.

Key words: galaxies: abundances – galaxies: evolution – galaxies: formation.

1 INTRODUCTION

James Webb Space Telescope (*JWST*)/Near Infrared Spectrograph (NIRSpec; P. Jakobsen et al. 2022) observations of high-redshift ($z > 1$) star-forming galaxies (SFGs) have enabled direct determination (via reliable detections of temperature-sensitive auroral lines) of their interstellar medium (ISM) abundances of various light elements (e.g. Y. Isobe et al. 2023; N. S. J. Rogers et al. 2024; K. Z. Arellano-Córdova et al. 2025a; S. Bhattacharya et al. 2025b; E. Cataldi et al. 2025; M. Stiavelli et al. 2025). Of particular interest are those high-z SFGs that have been found to display high log(N/O) values (termed extreme N-emitters or N-loud galaxies) at relatively low O abundances, $12 + \log(\mathrm{O/H}) \leq 8$ (A. J. Cameron et al. 2023; Y. Isobe et al. 2023; A. J. Bunker et al. 2024; M. Castellano et al. 2024; R. Marques-Chaves et al. 2024; R. L. Sanders et al. 2024; D. Schaerer et al. 2024; M. W. Topping et al. 2024, 2025; B. Welch et al. 2024, 2025; K. Z. Arellano-Córdova et al. 2025a; M. Curti et al. 2025b; M. Stiavelli et al. 2025; Y. Zhang, T. Morishita & M. Stiavelli 2026). We adopt a standard definition of extreme N-emitters (hereafter 'N-emitters' for brevity) in this work as such SFGs with $\log(\mathrm{N/O}) \geq -1.1$.

Various theoretical scenarios have been suggested to explain the high N/O at low O abundances in these high-z SFGs. These include dilution by pristine gas between intermittent starbursts (C. Kobayashi & A. Ferrara 2024), enrichment from winds of Wolf–Rayet (WR) stars possibly coupled with clustered star formation (Y. Isobe et al. 2023; H. Fukushima & H. Yajima 2024; R. Marques-Chaves et al. 2024; T. E. Rivera-Thorsen et al. 2024), pollution from Population III star formation (D. Nandal, Y. Sibony & S. Tsiatsiou 2024b; M. Rossi et al. 2024; P. Senchyna et al. 2024; S. Tsiatsiou et al. 2024), tidal disruption of stars from encounters with black holes (Y. Zhang et al. 2026), ejecta from very massive stars (100–1000 $\mathrm{M}_\odot$) formed through collisions in dense clusters (J. S. Vink 2023), and supermassive stars ($\sim 10^4$ $\mathrm{M}_\odot$; C. Charbonnel et al. 2023; C. Nagele & H. Umeda 2023; D. Nandal et al. 2024a). We note that some identified N-emitters at high z are shown to host an active galactic nucleus (AGN, e.g. GS 3073; X. Ji et al. 2024). However, in this work, we are only interested in N-emitters that are SFGs.

At low redshifts, N/O has been routinely determined for individual bright H II regions within the Milky Way (MW; e.g. M. Peimbert & R. Costero 1969; R. H. Rubin 1969; C. Esteban & J. García-Rojas 2018) and nearby galaxies (e.g. NGC 6822: M. Peimbert & H. Spinrad 1970; M31, M101: C. Esteban et al. 2020), for the integrated spectra of galaxies (e.g. Y. I. Izotov et al. 2006), for

★ E-mail: s.bhattacharya3@herts.ac.uk

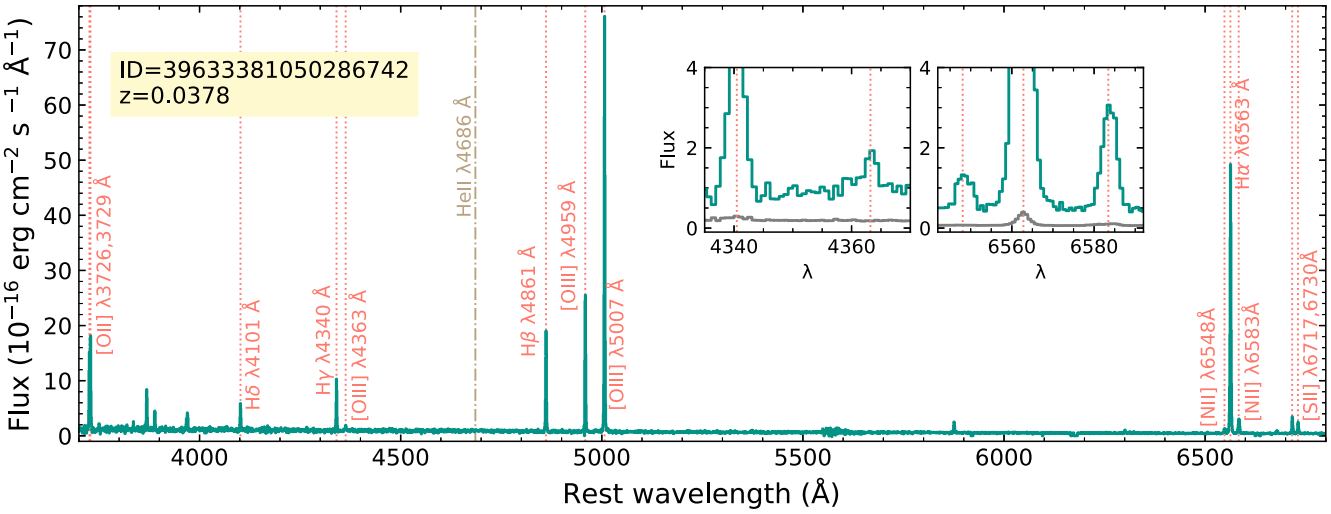

Figure 1. An example of the flux and wavelength calibrated spectrum (green) of an SFG observed by DESI (for the N-emitter No. 1 in Table 2; its DESI ID and redshift are noted). The emission lines utilized in this work are labelled in red. The expected position of the He II λ4686 Å line is marked (brown) but is not observed. The insets show the zoomed-in views around the H γ and [O III] λ4363 Å and H α and [N II] λλ6548, 6583 Å lines, respectively, both of which clearly show their detections. The uncertainty in the flux is marked in grey in these insets.

damped Lyman α systems (e.g. A. J. Battisti et al. 2012), as well as for stars in the MW (e.g. A. Ecuvillon et al. 2004). These determinations have shown that N/O is nearly constant with increasing O abundance when $12 + \log(\mathrm{O/H}) \approx 7.5$–8, and increases thereafter with increasing O abundance (M. A. Dopita et al. 2016; D. C. Nicholls et al. 2017). The increase is associated with enrichment from asymptotic giant branch (AGB) stars from initially ∼4–7 $\mathrm{M}_\odot$ stars (F. Vincenzo & C. Kobayashi 2018). At $12 + \log(\mathrm{O/H}) \leq 7.5$, N/O determinations remain sparser, although many blue compact dwarfs show slightly enhanced N relative to the near-constant values determined when $12 + \log(\mathrm{O/H}) \approx 7.5$–8 (e.g. I. A. Zinchenko et al. 2024).

In the Local Volume (<10 Mpc), extreme N-emitters are rare, with only the nuclear star-forming region in the blue compact dwarf galaxy Mrk 996 showing extremely high $\log(\mathrm{N/O}) \sim -0.15$ at low O abundances, $12 + \log(\mathrm{O/H}) \sim 7.9$ (B. L. James et al. 2009; E. Telles et al. 2014). Homogeneous spectroscopic survey of SFGs with the Sloan Digital Sky Survey (SDSS; H. Aihara et al. 2011) allowed direct N and O abundance measurements for 231 low-z galaxies (out to $z \sim 0.4$; Y. I. Izotov et al. 2006). However, only a handful of SFGs with $\log(\mathrm{N/O}) \geq -1.1$ were observed, with most of these having $12 + \log(\mathrm{O/H}) \geq 8$.

The Dark Energy Spectroscopic Instrument (DESI; DESI Collaboration 2022) on the Mayall 4-m Telescope at Kitt Peak National Observatory has carried out a ∼9000 deg^2 optical survey of galaxies over its first 13 months of operation, with data made publicly available through the Data Release 1 (DR1; DESI Collaboration 2025). This allows a renewed opportunity to conduct a homogeneous spectroscopic search for SFGs to directly determine their N and O abundances, but now over wider and potentially deeper scales than SDSS.

In this paper, we obtain direct N and O abundances for a sample of DESI DR1 SFGs at $z < 0.5$, to identify a homogeneous sample of N-emitters in the local Universe. Using galactic chemical evolution (GCE) models, we then constrain the physical processes that caused the observed high N/O values for the SFGs in our sample, to subsequently gain insight into the origin of N-emitters at high z. Our sample selection (including AGN exclusion) and direct abundance determination are described in Section 2. We explore the $12 + \log(\mathrm{O/H})$ versus $\log(\mathrm{N/O})$ plane for DESI DR1 SFGs and identify N-emitters in Section 3. We compare our identified N-emitters with literature N-enriched SFGs, both at low z and high z, in Section 4. Using GCE models, we draw inferences on the origin of N-emitters in Section 5. We conclude in Section 6.

2 SAMPLE SELECTION AND ABUNDANCE DETERMINATION

2.1 DESI DR1 value-added catalogue data

DESI enables multi-object spectroscopy with 5000 fibres (each 1.5 arcsec in diameter) over a 3.2° diameter field of view. The light from each fibre is split into the blue (3600–5550 Å; R = 2000–3200), red (5550–6560 Å; R = 3200–4100), and infrared (6560–9800 Å; R = 4100–5000) arms of a spectrograph, providing continuous wavelength coverage over the specified optical range. An example DESI spectrum of an SFG is shown in Fig. 1.

The DESI main survey is intended to be a 5-yr observational program targeting 30 million pre-selected galaxies across one-third of the night sky in order to measure redshifts. DESI DR1 consists of all data acquired during the first 13 months of the DESI main survey and uniform reprocessed DESI survey validation data that had been previously made publicly available as the DESI Early Data Release (EDR; DESI Collaboration 2024). The DESI DR1 main survey includes high-confidence redshifts for 18.7 million sources, of which 13.1 million are spectroscopically classified as galaxies.

In this work, we utilize the stellar mass and emission-line value-added catalogue (VAC)[1] from DESI DR1 (Zou et al., in preparation; consistent with H. Zou et al. 2024 for EDR). This VAC provides the position (RA, Dec.), spectroscopic redshift value (z), stellar mass (M_*), star formation rate (SFR)

[1]See https://data.desi.lbl.gov/doc/releases/dr1/vac/stellar-mass-emline for details.

Table 1. Sample selection of DESI DR1 galaxies in this work, with each subsequent sample being a subset of the former.

Sample	No. of galaxies
All targets in DESI DR1 VAC	14 706 085
Those of the above with $z \leq 0.4915$; flux/$\delta_{\rm flux}$ ([O III] 4363 Å, [O III] 5007 Å, Hβ) ≥ 3; flux ([N II] 6583 Å) > 0	9209
Those of the above that are SFGs, following AGN exclusion, with $z \geq 0.032$ and O abundances computed (for Fig. 2)	1815
Those of the above with flux/$\delta_{\rm flux}$ ([N II] 6583 Å) ≥ 3 and N and O abundances computed (in Fig. 3)	944
Those of the above with log(N/O) ≥ -1.1	19

and emission-line flux measurements for all sources classified as galaxies in DESI DR1 with reliable redshift measurements (see Table 1). For each source, following absorption correction through continuum fitting performed by the stellar spectral synthesis code STARLIGHT (R. Cid Fernandes et al. 2005), a predefined set of optical emission lines is measured by a single Gaussian fit. M_* is derived using the stellar population modelling software CIGALE (M. Boquien et al. 2019) from the broad-band g, r, z, $W1$, and $W2$ photometry from the DESI Legacy Imaging Surveys (A. Dey et al. 2019) and spectrophotometry of 10 artificial bands generated through convolution with DESI spectra (see H. Zou et al. 2024 for details). SFR is derived from the flux of the Hα line where available. Thus, while the tabulated SFR value only refers to the SFR within the region of the galaxy spanned on-sky by the fibre, the tabulated M_* value more broadly refers to the stellar mass of the source, even if its entire extent is not encompassed by the fibre.

We only utilize those tabulated emission-line fluxes for each galaxy from this VAC that are useful for direct O and N abundance measurements, i.e. [O II] $\lambda\lambda$3726, 3729 Å, Hδ, Hγ, [O III] λ4363 Å, Hβ, [O III] $\lambda\lambda$4959, 5007 Å, Hα, [N II] $\lambda\lambda$6548, 6583 Å, and [S II] $\lambda\lambda$6717, 6731 Å (see also Fig. 1). These line fluxes and their errors are utilized in selecting our sample of this work in Section 2.2. The abundance determination is discussed in Section 2.3.

2.2 Sample selection

We start from the ∼14.7 million targets in DESI DR1 classified as galaxies in the VAC (first row of Table 1) and make the following selections:

(i) As the red-most emission line of interest required for O and N abundance determination ([N II] λ6583 Å) was only tabulated for galaxies out to $z = 0.4915$, our sample is limited to this redshift. We further restrict our sample to those sources that have flux/$\delta_{\rm flux}$ ([O III] 4363 Å) ≥ 3 as a reliable line flux measurement of the temperature-sensitive [O III] λ4363 Å line is required for direct abundance determination. We find that this does not automatically imply that brighter [O III] 5007 Å and Hβ lines have signal-to-noise ratio (S/N) > 3. Thus, we additionally impose the selection criteria that flux/$\delta_{\rm flux}$ ([O III] 5007 Å, Hβ) ≥ 3. Given our interest in obtaining N abundances, we impose the selection criteria of flux ([N II] 6583 Å) > 0 (which also automatically selects only those objects with flux (Hα) > 0).[2] In this first instance, we thus have 9209 galaxies after our selection (second row of Table 1).

(ii) Visually checking these galaxies in the DESI Legacy Imaging Survey images,[3] we find that many of the lowest redshift sources classified as galaxies are actually individual H II regions in nearby spiral galaxies, having emission-line spectra. We thus impose an additional selection criterion of $z \geq 0.032$ to exclude such H II regions.[4] For the remaining sources, which are galaxies, we exclude candidate AGN by cross-matching with the DESI DR1 AGN/quasi-stellar object (QSO) VAC[5] (Juneau et al., in preparation). AGN candidates have been identified from the full DESI DR1 sample in this AGN/QSO VAC from various emission-line (L. J. Kewley et al. 2001; G. Kauffmann et al. 2003; R. Cid Fernandes et al. 2011; M. Shirazi & J. Brinchmann 2012; S. Juneau et al. 2014; K. Zhang & L. Hao 2018; D. R. Law et al. 2021) and infrared diagnostics (T. H. Jarrett et al. 2011; S. Mateos et al. 2012; D. Stern et al. 2012; R. J. Assef et al. 2018; H. F. M. Yao et al. 2020; R. E. Hviding et al. 2022). After removing these candidate AGN, the remaining emission-line galaxies in our sample are all SFGs based on the aforementioned emission-line and infrared diagnostics. For these SFGs, we proceed to abundance determination for O and N abundances (Section 2.3). Only those galaxies with reliable O abundances are included in the selection. This results in 1815 SFGs (third row of Table 1). This sample is used to check the consistency of our determined O abundance with previous works in Section 2.4.

(iii) N abundances are determined for a subsample of these SFGs where flux/$\delta_{\rm flux}$ ([N II] 6583 Å) ≥ 3, resulting in 944 SFGs that are studied in this work (fourth row of Table 1).

2.3 Abundance determination

Our abundance determination procedure using the Nebular Empirical Analysis Tool (NEAT; R. Wesson, D. J. Stock & P. Scicluna 2012) is laid out in detail in earlier papers (S. Bhattacharya et al. 2022, 2025a, b). We briefly describe the procedure here. For each SFG, NEAT utilizes an iterative procedure for calculating the intrinsic balmer decrement, c(Hβ), from flux-weighted ratios of Hα/Hβ, Hγ/Hβ, and Hδ/Hβ (as available), nebular temperature ($T_{\rm e}$) from the temperature-sensitive [O III] λ4363 Å line, and electron density ($n_{\rm e}$) from the density-sensitive [O II] $\lambda\lambda$3726, 3729 Å and [S II] $\lambda\lambda$6717, 6731 Å doublets (whichever are observed). We assume the extinction law of J. A. Cardelli, G. C. Clayton & J. S. Mathis (1989). For those galaxies where we do not observe the required doublets to determine $n_{\rm e}$, we assume $n_{\rm e} = 1000$ cm^{-3}, which is expected to have a negligible impact on the determined abundances (e.g. G. J. Ferland et al. 2013). Only those SFGs with c(Hβ) > 0, $T_{\rm e} < 35\,000$ K, and $n_{\rm e} < 10\,000$ cm^{-3} are considered to be reliable, and their direct abundances are determined (see also S. Bhattacharya et al. 2022, 2025a, b).

Direct O and N ionic abundances are determined from the measured fluxes of the O ([O II] $\lambda\lambda$3726, 3729 Å, [O III] $\lambda\lambda$4363,

[2] We find that a number of sources in the VAC have bright Hα and [N II] λ6583 Å lines (also verified visually from the released spectra), but have no tabulated errors. Not to exclude such sources, at least in the first instance, we refrain from S/N selection on these lines.

[3] https://www.legacysurvey.org

[4] A small number of dwarf galaxies could also be unfortunately excluded with this criterion.

[5] See https://data.desi.lbl.gov/doc/releases/dr1/vac/agnqso for details.

4959, 5007 Å) and N ([N II] λλ6548, 6583 Å) lines, respectively. Ionization correction factors (ICFs) for O are negligible when lines pertaining to both O^{2+} (i.e. [O III] λλ5007, 4959, 4363 Å) and O^{+} ([O II] λλ3727, 3729 Å) are observed. As the objective of this work is to check for N-enrichment, we can bypass the need for ICFs by directly obtaining log(N/O) as $\log(N^{+}/O^{+})$, which is considered to be a reasonable approximation for metal-poor galaxies (Y. I. Izotov et al. 2004).

2.4 Consistency with abundance determinations from DESI EDR

I. A. Zinchenko et al. (2024) had utilized the DESI EDR spectra to directly determine O abundances for 21 extremely metal-poor galaxies ($12 + \log(O/H) < 7.3$), 8 of which also had N abundances reported. Only 11 galaxies from their sample (including 3 with N abundances reported) are present in our selection of 1815 galaxies with reliable O abundances. Interestingly, none of these galaxies are among the 944 galaxies in our final selection that have reliable N abundances. This results from S/N > 3 considerations in the VAC for the [O III] 4363 Å line, which excludes 10 galaxies from I. A. Zinchenko et al. (2024) in our sample, and the remaining 11 galaxies are pruned as they all have no errors noted for the [N II] 6583 Å line in the VAC.

Visual confirmation of the DESI DR1 spectra of the galaxies from I. A. Zinchenko et al. (2024) gave the impression that the required [O III] 4363 Å and [N II] 6583 Å lines are present in the spectra as reported by the authors based on the EDR spectra, but these lines have low S/N, with the VAC conservatively assigning slightly higher errors than that determined by the authors. This is consistent with the presence of only seven of the galaxies from I. A. Zinchenko et al. (2024) being present in the metal-poor sample of H. Zou et al. (2024), who had utilized the DESI EDR VAC to report directly determined O abundances for 223 very metal-poor galaxies ($12 + \log(O/H) < 7.7$) in DESI EDR, 193 of which are within $z = 0.4915$.

Of these 193 galaxies, only 115 are present in our selection of galaxies with reliable O abundances. The ones excluded from our sample are primarily AGN candidates classified as such with the *Wide-field Infrared Survey Explorer* (*WISE*) colour-based AGN candidate selection criteria. While there is considerable overlap between AGN and SFGs in such *WISE* colour selections (e.g. T. H. Jarrett et al. 2011), we conservatively exclude all AGN candidates.

We compare our determined O abundances with those of the 11 galaxies in common with I. A. Zinchenko et al. (2024) and the 115 in common with H. Zou et al. (2024). Fig. 2 shows that we are consistent with the O abundances determined by I. A. Zinchenko et al. (2024) within the errors, but have mean O abundances lower by 0.06 dex than those determined by H. Zou et al. (2024), slightly more than the standard deviation of 0.044 dex, albeit still consistent within error. The offset likely stems from the choice of non-standard, albeit justified, atomic recombination and collision strength data by H. Zou et al. (2024), which is expected to result in their slightly higher O abundances. The abundance determination procedure, albeit using different software, is very similar between this work and that of I. A. Zinchenko et al. (2024). It is thus reassuring to determine consistent O abundances, as it bolsters the consistency between the line fluxes measured from the DESI spectra, and those reported in the VAC we use in this work.

For three SFGs, we can further compare the log(N/O) determined in this work with those reported by I. A. Zinchenko et al. (2024). We reiterate that these galaxies are not present in our final selection of 944 galaxies with reliable N abundances, as their [N II] 6583 Å lines flux errors are unreported in the VAC. Nevertheless, we assume a 10 per cent error on the reported flux in this line (an acceptable value visually checked with the spectra) to enable computation of the N abundances and thereby comparison with the reported values. Inset of Fig. 2 shows that our determined log(N/O) values are consistent with those reported by I. A. Zinchenko et al. (2024) for these three SFGs.

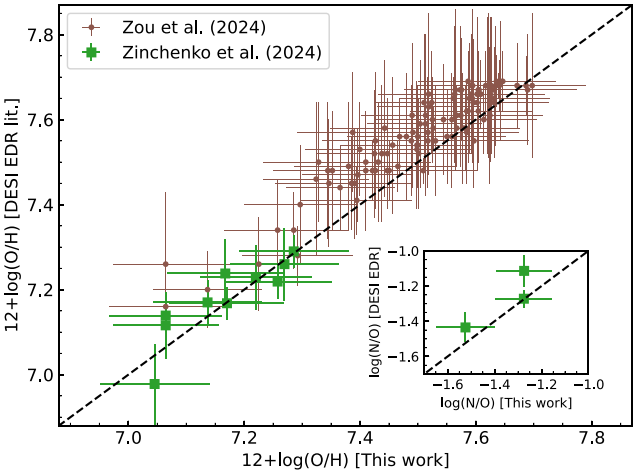

Figure 2. $12 + \log(O/H)$ abundances determined in this work compared to previous determinations (I. A. Zinchenko et al. 2024; H. Zou et al. 2024) from DESI EDR spectra. The 1:1 line is also marked. The inset shows the same for log(N/O).

3 ANALYSIS

3.1 The log(N/O) versus 12 + log(O/H) plane of SFGs

For the 944 SFGs with reliable O and N abundances directly determined in this work, we present their distribution in the $12 + \log(O/H)$ versus log(N/O) plane in Fig. 3. The running mean of log(N/O) is computed as a function of increasing $12 + \log(O/H)$ in a fixed window of 50 SFGs. The N/O increase at $12 + \log(O/H) > 8$, as per the local scaling relation,[6] is not clearly seen for our sample. This is probably due to a selection effect of our sample, where the [O III] λ4363 Å line flux (for the same [O III] λ5007 Å line flux) is inversely correlated with metallicity. So for any flux-limited spectroscopic survey, the [O III] λ4363 Å line is detected with higher S/N in relatively metal-poor galaxies (M. Curti et al. 2020). However, this is not a problem in this work for finding the low-z counterparts of high-z N-emitters, as most SFGs that are N-emitters at high z are at $12 + \log(O/H) < 8$.

Additionally, I. A. Zinchenko et al. (2024) made a compilation of metal-poor ($12 + \log(O/H) < 8$) low-z SFGs having direct N and O abundance determinations from the literature, and computed their mean log(N/O) as −1.48, shown with the dashed line in Fig 3 (see also E. Cataldi et al. 2025 for a very similar relation). We find that a number of our SFGs, especially those with $12 + \log(O/H) < 7.6$, have $\log(N/O) > -1.48$.

[6]This was computed from MW stars and H II regions in nearby galaxies (M. A. Dopita et al. 2016; D. C. Nicholls et al. 2017, see also the references for the original observations in Section 1).

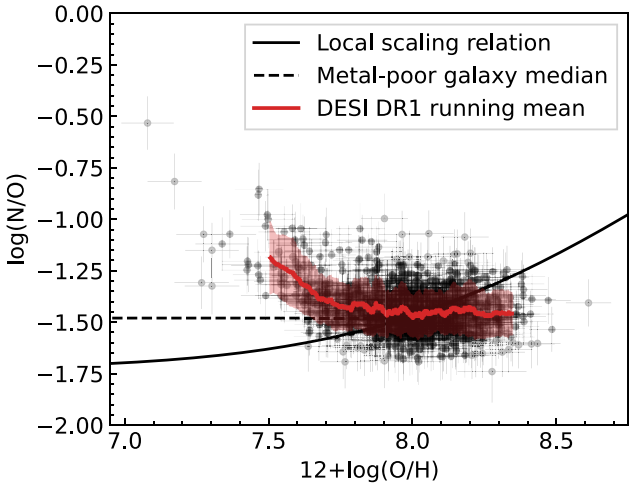

Figure 3. 12 + log(O/H) versus log(N/O) for the 944 DESI DR1 SFGs with our reliable O and N abundances. The uncertainties are marked with error bars. The running mean in log(N/O) as a function of 12 + log(O/H) is shown in red, with the 1σ uncertainty shaded. The local scaling relation (M. A. Dopita et al. 2016; D. C. Nicholls et al. 2017, solid line) is also marked, along with the median log(N/O) value for metal-poor galaxies computed by I. A. Zinchenko et al. (2024, dashed line).

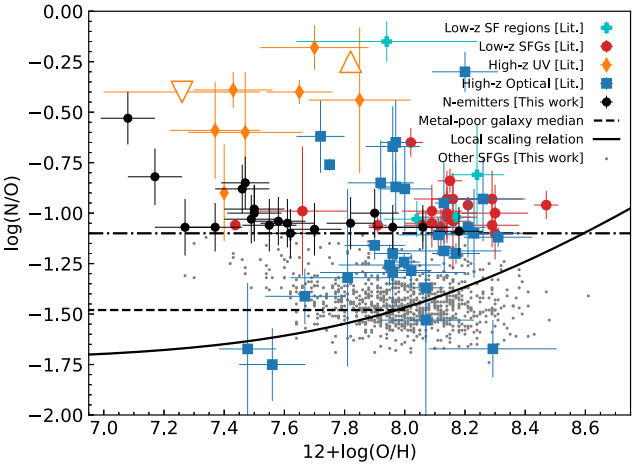

Figure 4. 12 + log(O/H) versus log(N/O) for the DESI DR1 944 SFGs with our reliable O and N abundances. 19 N-emitters (log(N/O) ≥ -1.1; those above the dot–dashed line) are marked in black (with their determined uncertainties), while the others are marked in grey. Different groups of literature sources are shown for comparison (see Section 4). Note that the upward triangle shows the lower limit for GN-z11, while the downward triangle shows the upper limit for GHZ2.

3.2 Extreme N-emitting SFGs in DESI DR1

We now make a selection of extreme N-emitters identified in SFGs at $z < 0.5$ from DESI DR1 in this work with the definition of log(N/O) > -1.1 (Section 1). The selection criteria are empirically made to allow for comparison with suitably large numbers of literature sources, both high z and low z ones, that have previously been studied for N-enhancement (discussed further in Sections 4.1 and 4.2).

As a result, we find 19 extreme N-emitters identified in our sample with log(N/O) > -1.1 (the last row of Table 1). They are highlighted in the 12 + log(O/H) versus log(N/O) plane in Fig. 4 (black dots with error bars) and their RGB image cutouts are shown in Fig. 5. While most of these SFGs are completely within the on-sky angular extent of the DESI fibre, some of them at low redshifts only have their central regions within the fibre. Their IDs, positions, redshifts, stellar masses, SFRs, and computed 12 + log(O/H) and log(N/O) are listed in Table 2. Fig. 1 shows the spectrum of the N-emitter No. 1 in Table 2 with clear detection of the auroral [O III] λ4363 Å line as well as the [N II] $\lambda\lambda$6548, 6583 Å lines. The spectra for the other 18 N-emitters are presented in Figs A1 and A2 and discussed in Appendix A.

Given the small number of such galaxies identified in our sample of 944 SFGs with reliable O and N abundances, we compute the fraction and uncertainty (95 per cent confidence interval) in the fraction of N-emitters, using the binomial proportion confidence interval obtained with the Wilson score interval method (E. B. Wilson 1927). We find that 2.21 ± 0.91 per cent of DESI DR1 SFGs, with reliable O and N abundances obtained directly, are N-emitters.

It is particularly notable that the most extreme N-emitter in our sample (No. 6 in Table 2 with log(N/O) $= -0.53 \pm 0.13$) also has the lowest 12 + log(O/H) with 7.08 ± 0.09 and the highest stellar mass, log(M_*/M$_\odot$) $= 9.95 \pm 0.13$, with the abundance values representative of its central regions (No. 6 in Fig. 5). The SFGs with the second and third highest log(N/O) values (No. 4 and No. 14 in Table 2 with log(N/O) $= -0.82 \pm 0.13$ and -0.85 ± 0.13) are also quite massive with log(M_*/M$_\odot$) $= 9.48 \pm 0.11$ and 9.35 ± 0.16, respectively, being also amongst the SFGs with the lowest O abundances in our sample with 12 + log(O/H) $= 7.17 \pm 0.09$ and 7.47 ± 0.08, respectively. The lowest mass galaxy in our sample (No. 7 in Table 2 with log(M_*/M$_\odot$) $= 7.03 \pm 0.17$) also has the fourth highest log(N/O) $= -0.88 \pm 0.12$, with a low 12 + log(O/H) $= 7.46 \pm 0.09$.

3.3 Relationship with other physical quantities

Fig. 6(a) shows that our sample of the DESI DR1 SFGs with reliable O and N abundances consists primarily of relatively lower mass SFGs, with the majority having $M_* \sim 10^8$–10^9 M$_\odot$. The selection of metal-poor galaxies in our sample (see Section 3.1) in conjunction with the mass–metallicity relation of galaxies, whereby galaxies on average show increasing O abundances with increasing mass (e.g. B. E. J. Pagel & M. G. Edmunds 1981; C. A. Tremonti et al. 2004; M. Curti et al. 2020), results in very few massive galaxies being present in our sample. This is still the case, although the masses of SFGs in our sample are higher than those in the literature sample compiled by I. A. Zinchenko et al. (2024).

Fig. 7(a) clearly shows a near constant fraction of N-emitters at 10^7–10^9 M$_\odot$, with an increase at higher masses. We find statistically that 14.99 ± 7.97 per cent and 37.24 ± 32.69 per cent of SFGs are N-emitters with $M_* = 10^9$–$10^{9.5}$ M$_\odot$ and $M_* = 10^{9.5}$–10^{10} M$_\odot$, respectively. At the lowest masses, given the lack of N-emitters in our sample, we can statistically say that only up to ∼15 per cent and ∼50 per cent of SFGs may be N-emitters with $M_* = 10^{6.5}$–10^7 M$_\odot$ and $M_* = 10^6$–$10^{6.5}$ M$_\odot$, respectively.

Fig. 6(b) shows that N-emitters are present over a wide range of SFR values (log(SFR) ~ -1.2 to 1.2 M$_\odot$ yr^{-1}) with a near constant fraction (∼1–2.5 per cent; see Fig. 7b). Beyond this SFR range, where we find no N-emitters in our sample, yet we can statistically say that up to ∼16 per cent SFGs may be N-emitters.

Fig. 6(c) shows that almost the entire sample of DESI DR1 SFGs with reliable O and N abundances have high specific star formation rate (sSFR), with the bulk of the sample having sSFR ∼ 10^{-9}–$10^{-7.5}$ yr^{-1}, which are typical values for starburst galaxies.

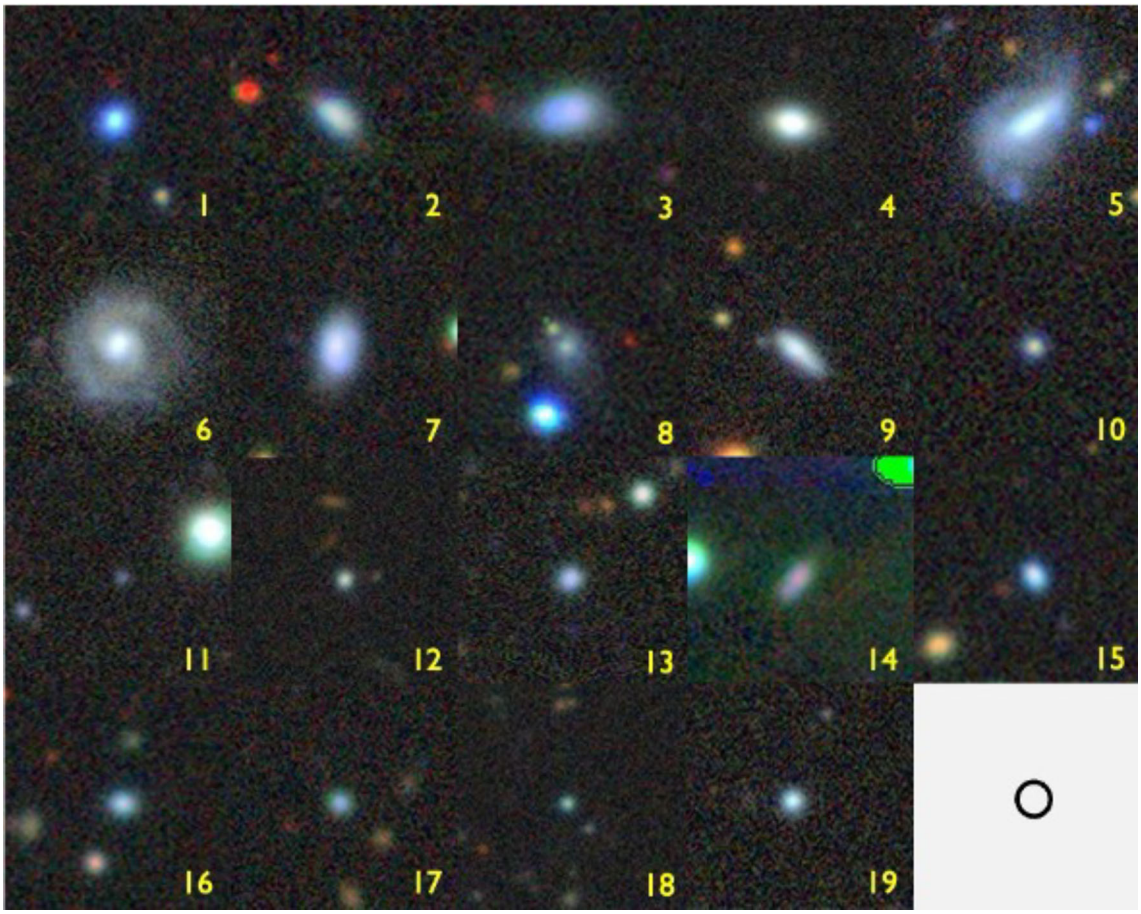

Figure 5. RGB image cutouts (10 arcmin × 10 arcmin) from data release DR10 of the DESI legacy imaging surveys for the 19 SFGs identified in this work, having considerably enriched N-abundances (log(N/O)≥−1.1). Their serial numbers from Table 2 are marked. The bottom-right panel shows the DESI fibre on-sky angular extent.

Table 2. Catalogued attributes and determined abundances of N-enriched galaxies (log(N/O) ≥ −1.1) identified in DESI DR1.

No.	DESI target ID	RA	Dec.	z	$\log(M_*/M_\odot)$	log(SFR)	$12+\log(O/H)$	log(N/O)
1	39633381050286742	191.859176	59.565488	0.0378	7.69 ± 0.18	-0.37 ± 0.17	7.96 ± 0.08	-1.07 ± 0.11
2	39633510662668308	100.838738	72.678735	0.0419	8.73 ± 0.14	-0.42 ± 0.24	7.37 ± 0.09	-1.07 ± 0.12
3	39632930795947980	199.982441	32.591007	0.0514	9.06 ± 0.14	-0.2 ± 0.22	7.49 ± 0.09	-1.03 ± 0.12
4	39627533284542216	58.21239	−10.411328	0.0581	9.48 ± 0.11	-0.15 ± 0.22	7.17 ± 0.09	-0.82 ± 0.13
5	39628209783834902	157.065201	17.867498	0.069	7.75 ± 0.03	0.39 ± 0.03	7.9 ± 0.08	-1.0 ± 0.12
6	39627850667526584	330.368151	2.403119	0.094	9.95 ± 0.13	0.93 ± 0.23	7.08 ± 0.09	-0.53 ± 0.13
7	39627697579625487	204.416316	−3.658184	0.0958	7.03 ± 0.17	-0.99 ± 0.21	7.46 ± 0.09	-0.88 ± 0.12
8	39633071447737239	118.114262	39.782491	0.096	9.11 ± 0.12	-0.27 ± 0.25	7.58 ± 0.09	-1.04 ± 0.12
9	39627836318813655	195.157633	2.079406	0.0984	9.37 ± 0.14	0.3 ± 0.26	7.82 ± 0.08	-1.05 ± 0.12
10	39633368454794121	181.353369	58.415714	0.1134	8.95 ± 0.15	-0.08 ± 0.28	7.5 ± 0.09	-1.0 ± 0.14
11	39627914379004562	173.883709	5.295752	0.1186	7.44 ± 0.22	-0.37 ± 0.25	7.5 ± 0.1	-0.98 ± 0.12
12	39627646585280675	36.837817	−5.867579	0.1257	8.0 ± 0.22	0.46 ± 0.16	8.18 ± 0.08	-1.09 ± 0.12
13	39628035053326862	228.697273	10.164711	0.127	8.76 ± 0.17	0.22 ± 0.26	7.27 ± 0.1	-1.07 ± 0.13
14	39633203069193270	98.286538	47.251371	0.1336	9.35 ± 0.16	1.18 ± 0.18	7.47 ± 0.08	-0.85 ± 0.13
15	39633039701053482	214.447961	37.948368	0.1359	9.21 ± 0.16	0.48 ± 0.25	7.7 ± 0.09	-1.08 ± 0.13
16	39633058315373292	188.542699	38.966799	0.1659	9.27 ± 0.14	0.38 ± 0.24	7.62 ± 0.09	-1.1 ± 0.12
17	39627911006784144	332.289797	5.081961	0.1734	9.01 ± 0.17	0.23 ± 0.27	7.55 ± 0.09	-1.06 ± 0.12
18	39627869588029634	18.529157	3.598735	0.2594	7.99 ± 0.14	0.54 ± 014	8.06 ± 0.09	-1.07 ± 0.11
19	39627763539249582	177.116195	−1.030106	0.269	9.33 ± 0.14	0.8 ± 0.21	7.61 ± 0.09	-1.05 ± 0.12

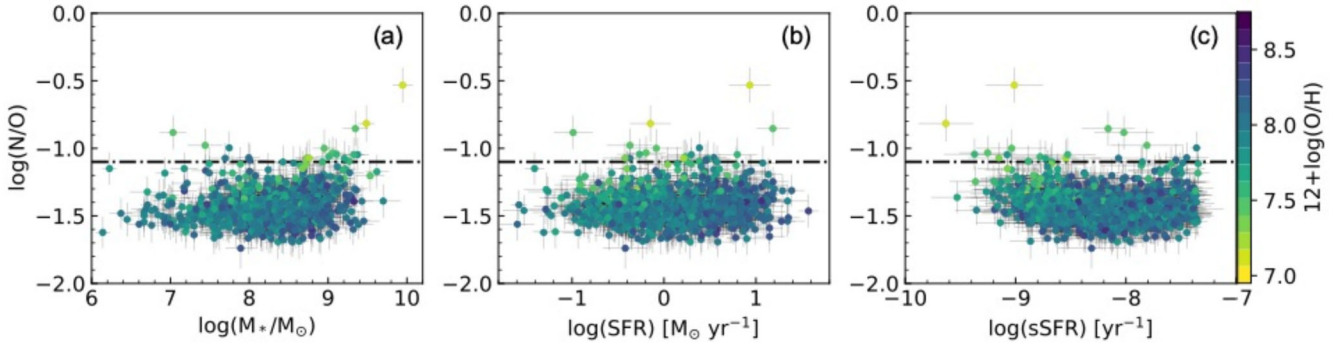

Figure 6. (a) Stellar mass versus log(N/O) for the DESI DR1 SFGs with reliable O and N abundances. The uncertainties are marked. The DESI DR1 SFGs are coloured by their 12 + log(O/H). The dash–dot line shows log(N/O) = −1.1, the demarcation line of N-emitters. (b) Same as panel (a), but now showing SFR versus log(N/O). (c) Same as panel (a), but now showing sSFR versus log(N/O).

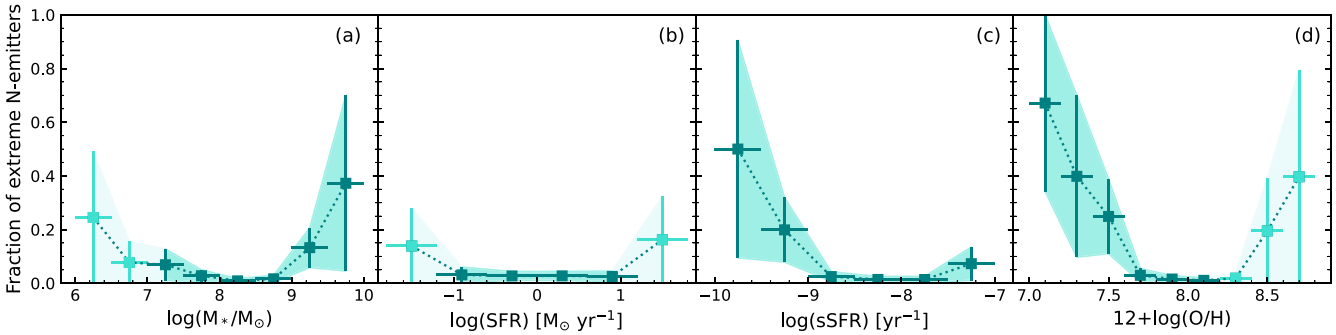

Figure 7. The fraction of N-emitters as a function of binned (a) stellar mass, (b) SFR, (c) sSFR, and (d) 12 + log(O/H). The fractions and uncertainties (95 per cent confidence interval) for the fraction of N-emitters in each bin are computed using the binomial proportion confidence interval obtained with the Wilson score interval method (E. B. Wilson 1927). Points marked with a darker shade have N-emitters identified in our sample in the respective parameter bin, while those with a lighter shade have no N-emitters identified (see Section 3.3 for more details).

While the N-emitters span the full range of sSFR values, it is clear from Fig. 7(c) that the lowest sSFR bins hold a higher fraction of N-emitters. This is consistent with the increased fraction of N-emitters at higher M_* but spanning a range of SFR values.

Fig. 7(d) shows the fraction of N-emitters as a function of binned 12 + log(O/H). As already shown in Fig. 3, it is clear that the fraction of N-emitters increase with decreasing O abundance.

4 COMPARISON WITH LITERATURE EXTREME N-EMITTING STAR-FORMING GALAXIES

4.1 Comparison with low-redshift extreme N-emitting SFGs

Enhancement of N/O in metal-poor SFGs has been previously reported (e.g. N. G. Guseva et al. 2011; E. Pérez-Montero et al. 2011; N. Kumari et al. 2018). Various mechanisms can be responsible for the enhanced N/O ratios at low metallicity, including localized nitrogen enrichment of the ISM by WR stars (N. Kumari et al. 2018), inflow of metal-poor gas (J. Köppen & G. Hensler 2005), varying star formation efficiency (E. Pérez-Montero et al. 2011), and initial mass function (IMF; F. Vincenzo et al. 2016).

Fig. 4 also shows the four known star-forming regions in nearby galaxies that show log(N/O) > −1.1 (cyan plus symbol). These are the nucleus of Mrk 996 (B. L. James et al. 2009; E. Telles et al. 2014), the centre of NGC 5253 (A. Monreal-Ibero, J. R. Walsh & J. M. Vílchez 2012), Region 2 in NGC 4670 (N. Kumari et al. 2018), and Region 2 in UM 448 (B. L. James et al. 2013a). All four have been suggested to be N-enriched due to WR stars, with Mrk 996 having the highest log(N/O) computed to date from optical N emission lines. Recently, V. Abril-Melgarejo et al. (2024) showed from studying individual H II regions spanning a range of ages in NGC 5253, young H II regions with ages ∼2–5 Myr exhibit high N/O (due to N-rich WR stars) decreasing with time, as the ionized gas might diffuse into the cold neutral gas on longer time-scales of ∼10–15 Myr.

Fig. 4 shows 20 blue compact dwarf galaxies (12 from Y. I. Izotov et al. 2006; one each from J. Brinchmann, D. Kunth & F. Durret 2008, N. G. Guseva et al. 2009 and Y. I. Izotov, T. X. Thuan & N. G. Guseva 2017; and five from K. Z. Arellano-Córdova et al. 2025a)[7] that have been found to have log(N/O) > −1.1 (red circles). Only three of these SFGs (J0519+0007, N. G. Guseva et al. 2009; J1205+4551, Y. I. Izotov et al. 2017; J0944+3442, K. Z. Arellano-Córdova et al. 2025b) have 12 + log(O/H) < 8. Their

[7]Recently, K. Z. Arellano-Córdova et al. (2025b) reported 10 galaxies with log(N/O) > −1.1. Among these, J0036−3333 is a well-known galaxy, Haro 11, whose resolved star-forming regions have been studied by B. L. James et al. (2013b), and none of its three star-forming knots have log(N/O) > −1.1. J0127−0619 and J0823+2806 are already included in this work as Mrk 996 and the SFG from J. Brinchmann et al. (2008), respectively. J0808+3948 and J1253−0312, the latter in common with Y. I. Izotov et al. (2006), are AGNs. The remaining five galaxies are plotted in Fig. 4.

log(N/O) values are among the lowest compared to the N-emitters in our sample. Note that, including Mrk 996 and these three SFGs, only four SFGs were previously known to be metal-poor ($12 + \log(O/H) < 8$) N-emitters at low z; our work adds a further 17 such metal-poor N-emitters in the local Universe (see Table 1).

We try not to include AGN at all in Fig. 4. There are five more blue compact dwarf galaxies that had previously been reported as SFGs with $\log(N/O) > -1.1$ in the literature (three from Y. I. Izotov et al. 2006; J0808+3948 from K. Z. Arellano-Córdova et al. 2025b; and HS 0837+4717 from S. Pustilnik et al. 2004). However, later, these are confirmed to be AGN either from X-ray follow-up (K. L. Birchall, M. G. Watson & J. Aird 2020), mid-infrared variability (A. Aravindan et al. 2024), optical-continuum variability (C. J. Burke et al. 2021), *WISE* colours (E. L. Lambrides et al. 2019), or spatially resolved spectroscopy (M. Mezcua & H. Domínguez Sánchez 2024). In addition, we find one more object from Y. I. Izotov et al. (2006) with $\log(N/O) > -1.1$ that is part of DESI DR1 but noted as an AGN candidate due to its *WISE* colours.

4.2 Comparison with high-redshift SFGs with log(N/O) determinations

Fig. 4 shows each of the high-z SFGs with log(N/O) determinations from optical N lines reported to date (blue squares). These include five SFGs from M. Stiavelli et al. (2025) at $z\sim$ 3.2–6.3, five from R. L. Sanders et al. (2024) at $z\sim$ 3.3–6, one from R. Marques-Chaves et al. (2025) at $z = 6.2$, one from Y. Zhang et al. (2026) at $z = 4.694$, one from N. S. J. Rogers et al. (2024) at $z = 2.963$, two from K. Z. Arellano-Córdova et al. (2025a) at $z\sim$ 5.2, 10 from D. Scholte et al. (2025) at $z\sim$ 1.8–4.9, one from B. Welch et al. (2024) at $z = 1.329$, two star-forming regions in an SFG at $z = 6.85$ (J. Scholtz et al. 2025), and the Lyman-continuum leaking star-forming region in the Sunburst Arc at $z = 2.37$ (B. Welch et al. 2025). 11 of these determinations have $\log(N/O) > -1.1$ (one from M. Stiavelli et al. 2025; all five from R. L. Sanders et al. 2024; one from Y. Zhang et al. 2026; one from B. Welch et al. 2024; two from K. Z. Arellano-Córdova et al. 2025a; and the star-forming region in the Sunburst Arc). J0217−0208 from R. Marques-Chaves et al. (2025) at $z = 6.2$ has the highest $\log(N/O) = -0.3 \pm 0.1$ among these SFGs. Note that E. Cataldi et al. (2025) also showed some additional N-emitters at cosmic noon with deep *JWST*/NIRSpec spectra.

The low-z N-emitters identified in this work have similar log(N/O) values with those at high z, albeit at lower O abundances. Particularly, the low-z N-emitters with high stellar mass ($M_* > 10^9$ $M_\odot$) also occupy a similar mass range as the high-z SFGs. It thus seems reasonable to consider that the mechanisms driving such high log(N/O) values are similar among both samples (see Section 5 for discussion).

Fig. 4 also shows each of the high-z SFGs with log(N/O) determinations from ultraviolet (UV) N lines reported to date (orange diamonds and triangles). There are seven such SFGs: A1703-zd6 ($z = 7.0435$; M. W. Topping et al. 2025), RXC J2248-ID ($z = 6.1057$; M. W. Topping et al. 2024), GLASS 150008 ($z = 6.23$; Y. Isobe et al. 2023), CEERS 1019 ($z = 8.68$; R. Marques-Chaves et al. 2024), GN-z9p4 ($z = 9.38$; D. Schaerer et al. 2024), GN-z8-LAE ($z = 8.28$; R. Navarro-Carrera et al. 2025), and GN-z9-0 ($z = 9.43$; M. Curti et al. 2025b). Also based on UV N lines, GN-z11 at $z = 10.6$ has been estimated to have $\log(N/O) \geq -0.25$ (A. J. Cameron et al. 2023), while GN-z2 at $z = 12.34$ has been estimated to have $\log(N/O) \leq -0.4$ (M. Castellano et al. 2024).

It is notable from Fig. 4 that all UV-based determinations of N/O result in high values that are well above $\log(N/O) = -1.1$. They are placed among the most extreme N-emitters identified in this work (No. 6 in Table 2 and Fig. 5). Only the nuclear region of Mrk 996 resembles CEERS 1019 in that it has $\log(N/O) = -0.18 \pm 0.11$. Note that, however, it has been widely suggested (e.g. M. Stiavelli et al. 2025) that the log(N/O) obtained from UV N lines is overestimated, potentially by ∼0.3–0.4 dex relative to the optical benchmark (Z. Martinez et al. 2025).

5 PROBING THE NATURE OF EXTREME N-EMITTERS AT LOW REDSHIFT WITH GCE MODELS

The low-z N-emitters identified in this work span a range of masses and sSFR (Section 3.3), but the most massive ones tend to have low sSFR and markedly low $12 + \log(O/H)$ as shown in Fig. 6. The lower mass ones span a wider range of sSFR with low $12 + \log(O/H)$. We here construct GCE models to explain the log(N/O) versus $12 + \log(O/H)$ parameter space spanned by N-emitters at low z identified in this work, which will help in understanding N-emitters at high z.

Together with the latest nucleosynthesis yields, classical one-zone GCE models have been instrumental in developing our understanding of chemical enrichment processes in galaxies (e.g. C. Kobayashi, A. I. Karakas & H. Umeda 2011; K. Nomoto, C. Kobayashi & N. Tominaga 2013; F. Matteucci 2021). Such GCE models have primarily been constrained by elemental abundance determinations of stars in the MW (e.g. M. R. Hayden et al. 2015) showing that an interplay of core-collapse supernovae (CCSNe, including hypernovae), Type Ia supernovae (SNe Ia) and AGB stars can explain the determined abundances of nearly all elements in the solar neighbourhood (C. Kobayashi, A. I. Karakas & M. Lugaro 2020b). The same chemical enrichment mechanisms, but paired with a distinct star formation history (M. Arnaboldi et al. 2022; C. Kobayashi et al. 2023), can reproduce the observed O and Ar elemental abundances for planetary nebulae in the disc of the Andromeda galaxy (S. Bhattacharya et al. 2022). GCE models have also been constrained by elemental abundance determinations of stars in MW dwarf spheroidal satellite galaxies, uncovering the potential role played by sub-Chandrasekhar mass SNe Ia (sub-Ch SNe Ia) in the chemical enrichment of such low-mass metal-poor galaxies (C. Kobayashi, S.-C. Leung & K. Nomoto 2020a).

C. Kobayashi & A. Ferrara (2024) utilized GCE models, with an intermittent star formation history having two strong starbursts separated by a quiescent phase lasting ∼100 Myr and having outflows, to provide a possible explanation for the extreme N-enhancement of GN-z11. It is important to note that the quiescent phase is not particularly required, and the essential factor is the dual burst (see four other models in their fig. 4 of appendix). Akin to what has been observed for NGC 5253 by V. Abril-Melgarejo et al. (2024), WR stars temporarily (<1 Myr) enhance N abundances in GN-z11 following the second burst to become the dominant enrichment source.

5.1 Constructing GCE models

We construct a new set of GCE models using the GCE code by C. Kobayashi, T. Tsujimoto & K. Nomoto (2000) but including the latest nucleosynthesis yields of AGB stars, super-AGB stars, CCSNe (C. Kobayashi et al. 2020b), SNe Ia, and sub-Ch SNe Ia

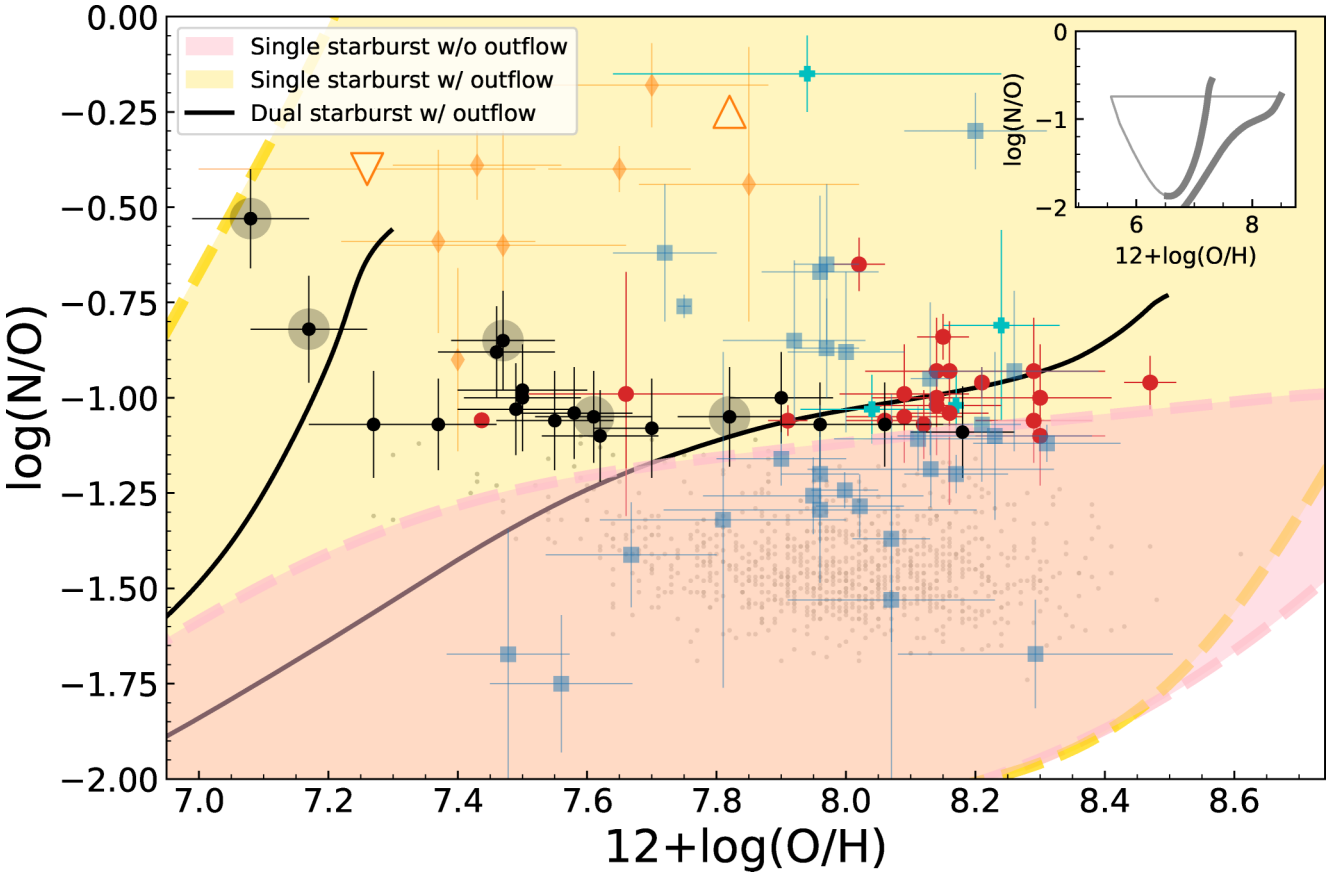

Figure 8. Same as Fig. 4, but with the locus traced by our GCE models marked (see Section 5 for details). The five most massive extreme N-emitters (Table 2) are encircled. The inset shows 12 + log(O/H) versus log(N/O) with an extended *x*-axis compared to the main plot, showing the complete locus traced by the dual starburst model. The locus positions accompanied by appreciable star formation are marked by the thicker solid lines (see Section 5 for details).

(C. Kobayashi et al. 2020a), as well as WR stars (C. Kobayashi & A. Ferrara 2024). The standard IMF from P. Kroupa (2008) is adopted for 0.01–120 $M_\odot$. Note that the SN Ia model is taken from C. Kobayashi & K. Nomoto (2009), which includes a metallicity effect of Chandrasekhar mass explosion in single degenerate systems (C. Kobayashi et al. 1998). Sub-Chandrasekhar mass explosions from single and double degenerate systems are also included.[8] However, they do not affect N/O ratios at all. It is important to note the model can well reproduce the observed elemental abundances (from C to Zn) in the solar neighbourhood (C. Kobayashi et al. 2020b).

The GCE models include exponential inflow (with time-scale τ_i), SFR proportional to the gas fraction (τ_s), and outflow rate also proportional to the gas fraction (τ_o). See C. Kobayashi (2025) for the formula (equations 9, 10, and 12). Three sets of models are constructed, including a multiple starburst. Massive stars formed in the first burst in each of the models explode as CCSNe, enriching the ISM with O, while N is contributed at early times from WR stars and at later times from AGB stars. This causes the increase of N/O toward higher metallicities (e.g. O abundances) in all models. The model predictions are shown in Fig. 8 and can be summarized as follows:

(i) *Single starburst without outflow*. The pink shaded area in Fig. 8 shows the range of single-burst models for 3 Gyr after the onset of star formation, with varying star formation time-scale from $\tau_s = 0.1$ to 30 Gyr. The model with $\tau_s = 0.1$ Gyr corresponds to the highest star formation efficiency among the models and is located at the metal-rich edge. The inflow time-scale is fixed to $\tau_i = 0.1$ Gyr as it does not change the elemental abundance tracks at all.

(ii) *Single starburst with outflow*. The yellow shaded area in Fig. 8 shows single-burst strong-outflow models with $\tau_o = \tau_i = 0.1$ Gyr, again varying τ_s from 0.1 to 30 Gyr, which can produce high N/O ratios over a wide range of O/H. With outflows, N/O ratios become higher due to loss of O and can explain *all* high N/O values in SFGs. Note that, with a longer τ_o value, i.e. weaker outflow, the yellow area approaches the pink area. With these outflows, N/O becomes higher mainly with the delayed N enrichment from AGB stars.

(iii) *Dual starburst with outflow*. There is another way to produce high N/O at low metallicities – a dual starburst (C. Kobayashi & A. Ferrara 2024). The black solid lines in Fig. 8 show the star formation (observable) episodes of a dual starburst model; both bursts have the same star formation time-scale

[8]Equation (2) of C. Kobayashi & K. Nomoto (2009) is also used for sub-Ch-mass SNe Ia, but with different secondary mass ranges; 0.835–1.9 $M_\odot$ for single degenerate systems (C. Kobayashi, K. Nomoto & I. Hachisu 2015) and 1.8–7.95 $M_\odot$ for double degenerate systems, depending on the metallicity.

$\tau_s = 10$ Gyr, but the infall time-scales are $\tau_i = 0.1$ and 0.2 Gyr, respectively, and the outflow time-scales are $\tau_o = 0.5$ and 0.1 Gyr, respectively, which results in the second burst being only a third of the SFR of the first one. The full evolutionary track is shown in the inset of Fig. 8 in the $12 + \log(O/H)$ versus $\log(N/O)$ plane, where the thick solid lines show the locus associated with each of the bursts of star formation that have an observable number of stars. The loop is the signature of ISM dilution following gas infall prior to the start of the second burst. During the first burst, even with moderate outflow, the model locus traces an increasing N/O with rapidly increasing O/H (the rightmost thick line). Then, the secondary inflow of primordial gas dilutes the ISM, suddenly decreasing O/H (the narrow horizontal line). CCSNe from the secondary star burst increase O, causing the rapid decrease of N/O while increasing O/H (the leftmost narrow line). Finally, AGB stars from secondary starburst enhance N, causing the increase of N/O (the inner thick line).

Note that the dual burst model track is similar but not as bursty as that for GN-z11 in C. Kobayashi & A. Ferrara (2024); the extra enhancement from WR stars before the O production from CCSNe is included but is not seen. Also, for ∼40 Myr after the onset of the first burst, AGB stars do not contribute to chemical evolution, which is important to note for very high-z galaxies.

5.2 GCE model-based inference

The aforementioned models provide considerable insight into the nature of extreme N-emitters, especially at low z.

The single starburst models without outflow (Fig. 8, pink) can well reproduce the local scaling relation (see Fig. 4) where observed N/O ratios increase with increasing O abundances, as well as the bulk of SFGs with O and N abundances determined in this work. However, they cannot explain the N-emitters, especially at low metallicities, $12 + \log(O/H) < 8$.

Among our N-emitters, those with relatively low stellar mass (approximately $M_* < 10^9$ $M_\odot$; see Table 2) can be explained with the single starburst models with outflow (Fig. 8, yellow). As they are dwarf galaxies, strong outflow from star formation activity is expected due to their small gravitational potential well. It is important to note that we do not necessarily expect an ongoing outflow signature to be present in the spectra of these SFGs. Our GCE models show that outflows during the evolution of these galaxies result in high N/O at a given O/H with delayed N-enrichment from AGB stars. However, for the non-AGN high-mass galaxies such a strong outflow is not expected.

For the massive N-emitters in our sample (approximately $M_* > 10^9$ $M_\odot$; see Table 2), with the five most massive ones marked in Fig. 8, a dual starburst with outflow is more plausible. This particular model assumes the peak SFR is lower in the second burst, which is also consistent with cosmological growth of galaxies. Generally, dual starbursts with similar outflows can explain the high N/O ratios, too. Having already experienced a previous burst of star formation, the galaxy formed in the dual starburst case will likely be more massive and thus have lower sSFR, consistent with the properties of extreme N-emitting SFGs in our sample (see Section 3.3 and Fig. 7c).

Given the aforementioned scenarios for low-z galaxies, we find that sustained N-enhancement by AGB stars, in conjunction with the presence of outflows during the evolution of the galaxy, can explain the observed high N/O ratios of low-z N-emitters. Such a scenario may be applicable to the relatively massive high-z N-emitters at $z < 9$, when there has been sufficient time (>0.5 Gyr) for N-enrichment by AGBs, regardless of whether single, dual, or multiple episodes of starburst have occurred. The high-z N-emitters at $z > 9$, with UV-based N-abundances determined, require more rapid enrichment modes (<0.5 Gyr) like WR stars.

As we move to higher redshifts, galaxies have had shorter lifespans and so signatures of ongoing outflows may be present in the highest z N-emitters (albeit at $z < 9$). Indeed, J0217−0208 from R. Marques-Chaves et al. (2025) at $z = 6.2$, having $\log(N/O) = -0.3 \pm 0.1$, the highest of any high-z N-emitter with optical N-lines, shows signatures of strong outflows (broad components in several rest-optical emission lines combined with ALMA (Atacama Large Millimeter/submillimeter Array) detections of a massive, extended cold dust reservoir), consistent with N-enhancement from AGB stars in systems with strong outflows as per our proposed GCE models. The same is true for CEERS 1019 at $z = 8.68$, where outflows have recently been identified with NIRSpec integral field unit (S. Zamora et al. 2025).

Note again that WR stars are also included, but their instantaneous N-enhancement is not visible in the GCE models of this paper.[9] There is no detection of the He II λ4686 Å line, which is expected to accompany the characteristic blue bump in galaxies with WR stars (e.g. A. R. López-Sánchez & C. Esteban 2009; M. Curti et al. 2025a), in any of our extreme N-emitters (see Figs 1, A1, and A2). The He II λ4686 Å line also remains undetected in the stacked spectrum of our extreme N-emitters (see Appendix B). However, given the faintness of this line even for known galaxies with WR stars (e.g. A. R. López-Sánchez & C. Esteban 2009), any contribution of WR stars to the N-enhancement for the low-z SFGs remains unclear.

6 CONCLUSION

We obtain direct N and O abundances for a sample of 944 SFGs at $z < 0.5$ in DESI DR1, and find that 19 of these SFGs are N-emitters with $\log(N/O) > -1.1$ (Section 3.2). This is a fivefold increase in the number of metal-poor ($12 + \log(O/H) < 8$) low-z N-emitters (17 from our sample), as only four such SFGs were known previously (Section 4.1). Four of the N-emitters identified in this work have the lowest $12 + \log(O/H)$ values determined to date for such galaxies (Fig. 4). The most extreme N-emitter in our sample (No. 6 in Table 2 with $\log(N/O) = -0.53 \pm 0.13$) also has the lowest $12 + \log(O/H)$ with 7.08 ± 0.09 and the highest stellar mass, $\log(M_*/M_\odot) = 9.95 \pm 0.13$.

The homogeneous sample allows us to compute the N-emitter fraction of 2.21 ± 0.91 per cent. These N-emitters span a wide range of SFR values, but a marked number of them have higher stellar masses and low sSFR, as well as low O abundances (Fig. 6). In fact, the fraction of N-emitters increases with increasing mass, decreasing sSFR and decreasing O abundance (Fig. 7).

Constructing a new set of GCE models (Section 5), we show that single starburst models without outflows cannot explain the high $\log(N/O)$ values of the low-z N-emitters at $12 + \log(O/H) < 8$, and strong outflows are required (Fig. 8). However, such strong outflows are not very likely in our relatively massive non-AGN SFGs (approximately $M_* > 10^9$ $M_\odot$; see Table 2). For these galax-

[9] As a diagnostic test, we recompute the GCE model predictions by setting WR contribution to zero, and find no discernible change in the predicted N/O versus O/H plots for any of our models.

ies, dual starbursts with outflows better explain the high log(N/O) values.

We thus show that extreme N-emitters at low O abundances, such as those observed at high z, are also present in the local Universe, allowing us to gain significant insight into their chemical enrichment mechanisms. N-enrichment from AGB stars, coupled with strong outflows sometime during the lifetime of a galaxy in single and dual starbursts, is the likely driver of high log(N/O) in low-z N-emitters. Such enrichment mechanisms may also explain the high log(N/O) in high-z SFGs out to $z\sim 9$. A larger homogeneous sample across cosmic time with multi-object spectrographs on 8–10 m class ground-based telescopes, such as Subaru's Prime Focus Spectrograph and Very Large Telescope's Multi-Object Optical and Near-infrared Spectrograph, is required to probe the origin of N-emitters, as well as targeted observations with the *JWST*.

ACKNOWLEDGEMENTS

We thank the anonymous referee for their valuable suggestions. CK acknowledges funding from the UK Science and Technology Facilities Council through grant ST/Y001443/1. This research used data obtained with the Dark Energy Spectroscopic Instrument (DESI). DESI construction and operations are managed by the Lawrence Berkeley National Laboratory. This paper is based upon work supported by the U.S. Department of Energy Office of Science, Office of High-Energy Physics, under Contract No. DE-AC02-05CH11231, and by the National Energy Research Scientific Computing Center, a DOE Office of Science User Facility under the same contract. Additional support for DESI was provided by the U.S. National Science Foundation (NSF), Division of Astronomical Sciences under Contract No. AST-0950945 to the NSF's National Optical–Infrared Astronomy Research Laboratory; the Science and Technology Facilities Council of the United Kingdom; the Gordon and Betty Moore Foundation; the Heising-Simons Foundation; the French Alternative Energies and Atomic Energy Commission (CEA); the National Council of Humanities, Science and Technology of Mexico (CONAHCYT); the Ministry of Science and Innovation of Spain (MICINN), and by the DESI Member Institutions: www.desi.lbl.gov/collaborating-institutions. The DESI Collaboration is honoured to be permitted to conduct scientific research on I'oligam Du'ag (Kitt Peak), a mountain with particular significance to the Tohono O'odham Nation. Any opinions, findings, and conclusions, or recommendations expressed in this paper are those of the author(s) and do not necessarily reflect the views of the U.S. National Science Foundation, the U.S. Department of Energy, or any of the listed funding agencies.

DATA AVAILABILITY

Based on tabulated data publicly available at the DESI DR1 Data Release. GCE models can be shared upon reasonable request.

REFERENCES

Abril-Melgarejo V., James B. L., Aloisi A., Mingozzi M., Lebouteiller V., Hernandez S., Kumari N., 2024, ApJ, 973, 173
Aihara H. et al., 2011, ApJS, 193, 29
Aravindan A., Canalizo G., Secrest N., Satyapal S., Bohn T., 2024, ApJ, 975, 60
Arellano-Córdova K. Z. et al., 2025a, MNRAS, 540, 2991
Arellano-Córdova K. Z. et al., 2025b, MNRAS, 544, 1588
Arnaboldi M. et al., 2022, A&A, 666, A109
Assef R. J., Stern D., Noirot G., Jun H. D., Cutri R. M., Eisenhardt P. R. M., 2018, ApJS, 234, 23
Battisti A. J. et al., 2012, ApJ, 744, 93
Bhattacharya S. et al., 2022, MNRAS, 517, 2343
Bhattacharya S., Arnaboldi M., Kobayashi C., Gerhard O., Saha K., 2025a, preprint (arXiv:2505.01896)
Bhattacharya S., Arnaboldi M., Gerhard O., Kobayashi C., Saha K., 2025b, ApJ, 983, L30
Birchall K. L., Watson M. G., Aird J., 2020, MNRAS, 492, 2268
Boquien M., Burgarella D., Roehlly Y., Buat V., Ciesla L., Corre D., Inoue A. K., Salas H., 2019, A&A, 622, A103
Brinchmann J., Kunth D., Durret F., 2008, A&A, 485, 657
Bunker A. J. et al., 2024, A&A, 690, A288
Burke C. J. et al., 2021, Science, 373, 789
Cameron A. J., Katz H., Rey M. P., Saxena A., 2023, MNRAS, 523, 3516
Cardelli J. A., Clayton G. C., Mathis J. S., 1989, ApJ, 345, 245
Carnall A. C., 2017, preprint (arXiv:1705.05165)
Castellano M. et al., 2024, ApJ, 972, 143
Cataldi E. et al., 2025, preprint (arXiv:2512.07955)
Charbonnel C., Schaerer D., Prantzos N., Ramírez-Galeano L., Fragos T., Kuruvanthodi A., Marques-Chaves R., Gieles M., 2023, A&A, 673, L7
Cid Fernandes R., Mateus A., Sodré L., Stasińska G., Gomes J. M., 2005, MNRAS, 358, 363
Cid Fernandes R., Stasińska G., Mateus A., Vale Asari N., 2011, MNRAS, 413, 1687
Curti M., Mannucci F., Cresci G., Maiolino R., 2020, MNRAS, 491, 944
Curti M. et al., 2025a, preprint (arXiv:2509.06622)
Curti M. et al., 2025b, A&A, 697, A89
DESI Collaboration, 2022, AJ, 164, 207
DESI Collaboration, 2024, AJ, 168, 58
DESI Collaboration, 2025, preprint (arXiv:2503.14745)
Dey A. et al., 2019, AJ, 157, 168
Dopita M. A., Kewley L. J., Sutherland R. S., Nicholls D. C., 2016, Ap&SS, 361, 61
Ecuvillon A., Israelian G., Santos N. C., Mayor M., García López R. J., Randich S., 2004, A&A, 418, 703
Esteban C., García-Rojas J., 2018, MNRAS, 478, 2315
Esteban C., Bresolin F., García-Rojas J., Toribio San Cipriano L., 2020, MNRAS, 491, 2137
Ferland G. J. et al., 2013, Rev. Mex. Astron. Astrofis., 49, 137
Fukushima H., Yajima H., 2024, PASJ, 76, 1122
Guseva N. G., Papaderos P., Meyer H. T., Izotov Y. I., Fricke K. J., 2009, A&A, 505, 63
Guseva N. G., Izotov Y. I., Stasińska G., Fricke K. J., Henkel C., Papaderos P., 2011, A&A, 529, A149
Hayden M. R. et al., 2015, ApJ, 808, 132
Hviding R. E., Hainline K. N., Rieke M., Juneau S., Lyu J., Pucha R., 2022, AJ, 163, 224
Isobe Y. et al., 2023, ApJ, 959, 100
Izotov Y. I., Stasińska G., Guseva N. G., Thuan T. X., 2004, A&A, 415, 87
Izotov Y. I., Stasińska G., Meynet G., Guseva N. G., Thuan T. X., 2006, A&A, 448, 955
Izotov Y. I., Thuan T. X., Guseva N. G., 2017, MNRAS, 471, 548
Jakobsen P. et al., 2022, A&A, 661, A80
James B. L., Tsamis Y. G., Barlow M. J., Westmoquette M. S., Walsh J. R., Cuisinier F., Exter K. M., 2009, MNRAS, 398, 2
James B. L., Tsamis Y. G., Barlow M. J., Walsh J. R., Westmoquette M. S., 2013a, MNRAS, 428, 86
James B. L., Tsamis Y. G., Walsh J. R., Barlow M. J., Westmoquette M. S., 2013b, MNRAS, 430, 2097
Jarrett T. H. et al., 2011, ApJ, 735, 112
Ji X. et al., 2024, MNRAS, 535, 881
Juneau S. et al., 2014, ApJ, 788, 88
Kauffmann G. et al., 2003, MNRAS, 346, 1055
Kewley L. J., Dopita M. A., Sutherland R. S., Heisler C. A., Trevena J., 2001, ApJ, 556, 121
Kobayashi C., 2025, preprint (arXiv:2506.20436)

Kobayashi C., Ferrara A., 2024, ApJ, 962, L6
Kobayashi C., Nomoto K., 2009, ApJ, 707, 1466
Kobayashi C., Tsujimoto T., Nomoto K., Hachisu I., Kato M., 1998, ApJ, 503, L155
Kobayashi C., Tsujimoto T., Nomoto K., 2000, ApJ, 539, 26
Kobayashi C., Karakas A. I., Umeda H., 2011, MNRAS, 414, 3231
Kobayashi C., Nomoto K., Hachisu I., 2015, ApJ, 804, L24
Kobayashi C., Leung S.-C., Nomoto K., 2020a, ApJ, 895, 138
Kobayashi C., Karakas A. I., Lugaro M., 2020b, ApJ, 900, 179
Kobayashi C., Bhattacharya S., Arnaboldi M., Gerhard O., 2023, ApJ, 956, L14
Köppen J., Hensler G., 2005, A&A, 434, 531
Kroupa P., 2008, in Knapen J. H., Mahoney T. J., Vazdekis A., eds, ASP Conf. Ser. Vol. 390, Pathways Through an Eclectic Universe. Astron. Soc. Pac., San Francisco, p. 3
Kumari N., James B. L., Irwin M. J., Amorín R., Pérez-Montero E., 2018, MNRAS, 476, 3793
Lambrides E. L., Petric A. O., Tchernyshyov K., Zakamska N. L., Watts D. J., 2019, MNRAS, 487, 1823
Law D. R. et al., 2021, ApJ, 915, 35
López-Sánchez A. R., Esteban C., 2009, A&A, 508, 615
Marques-Chaves R. et al., 2024, A&A, 681, A30
Marques-Chaves R. et al., 2025, preprint (arXiv:2510.12411)
Martinez Z. et al., 2025, ApJ, 995, 204
Mateos S. et al., 2012, MNRAS, 426, 3271
Matteucci F., 2021, A&AR, 29, 5
Mezcua M., Domínguez Sánchez H., 2024, MNRAS, 528, 5252
Monreal-Ibero A., Walsh J. R., Vílchez J. M., 2012, A&A, 544, A60
Nagele C., Umeda H., 2023, ApJ, 949, L16
Nandal D., Regan J. A., Woods T. E., Farrell E., Ekström S., Meynet G., 2024a, A&A, 683, A156
Nandal D., Sibony Y., Tsiatsiou S., 2024b, A&A, 688, A142
Navarro-Carrera R., Caputi K. I., Iani E., Rinaldi P., Kokorev V., Kerutt J., 2025, ApJ, 993, 194
Nicholls D. C., Sutherland R. S., Dopita M. A., Kewley L. J., Groves B. A., 2017, MNRAS, 466, 4403
Nomoto K., Kobayashi C., Tominaga N., 2013, ARA&A, 51, 457
Pagel B. E. J., Edmunds M. G., 1981, ARA&A, 19, 77
Peimbert M., Costero R., 1969, Bol. Obser. Tonantzintla Tacubaya, 5, 3
Peimbert M., Spinrad H., 1970, A&A, 7, 311
Pérez-Montero E. et al., 2011, A&A, 532, A141
Pustilnik S., Kniazev A., Pramskij A., Izotov Y., Foltz C., Brosch N., Martin J. M., Ugryumov A., 2004, A&A, 419, 469
Rivera-Thorsen T. E. et al., 2024, A&A, 690, A269
Rogers N. S. J., Strom A. L., Rudie G. C., Trainor R. F., Raptis M., von Raesfeld C., 2024, ApJ, 964, L12
Rossi M., Romano D., Mucciarelli A., Ceccarelli E., Massari D., Zamorani G., 2024, A&A, 691, A284
Rubin R. H., 1969, ApJ, 155, 841
Sanders R. L., Shapley A. E., Topping M. W., Reddy N. A., Brammer G. B., 2024, ApJ, 962, 24
Schaerer D., Marques-Chaves R., Xiao M., Korber D., 2024, A&A, 687, L11
Scholte D. et al., 2025, MNRAS, 540, 1800
Scholtz J. et al., 2025, MNRAS, 539, 2463
Senchyna P., Plat A., Stark D. P., Rudie G. C., Berg D., Charlot S., James B. L., Mingozzi M., 2024, ApJ, 966, 92
Shirazi M., Brinchmann J., 2012, MNRAS, 421, 1043
Stern D. et al., 2012, ApJ, 753, 30
Stiavelli M. et al., 2025, ApJ, 981, 136
Telles E., Thuan T. X., Izotov Y. I., Carrasco E. R., 2014, A&A, 561, A64
Topping M. W. et al., 2024, MNRAS, 529, 3301
Topping M. W. et al., 2025, ApJ, 980, 225
Tremonti C. A. et al., 2004, ApJ, 613, 898
Tsiatsiou S. et al., 2024, A&A, 687, A307
Vincenzo F., Kobayashi C., 2018, MNRAS, 478, 155
Vincenzo F., Belfiore F., Maiolino R., Matteucci F., Ventura P., 2016, MNRAS, 458, 3466
Vink J. S., 2023, A&A, 679, L9
Welch B. et al., 2024, ApJ, 975, 196
Welch B. et al., 2025, ApJ, 980, 33
Wesson R., Stock D. J., Scicluna P., 2012, MNRAS, 422, 3516
Wilson E. B., 1927, J. Am. Stat. Assoc., 22, 209
Yao H. F. M. et al., 2020, ApJ, 903, 91
Zamora S. et al., 2025, preprint (arXiv:2512.09022)
Zhang K., Hao L., 2018, ApJ, 856, 171
Zhang Y., Morishita T., Stiavelli M., 2026, ApJ, 998, 141
Zinchenko I. A., Sobolenko M., Vílchez J. M., Kehrig C., 2024, A&A, 690, A28
Zou H. et al., 2024, ApJ, 961, 173

APPENDIX A: SPECTRA OF EXTREME N-EMITTERS

As in Fig. 1, the DESI spectra for the rest of N-emitters (Nos 2–18 in Table 2) are shown in Figs A1 and A2. The [N II] λλ6548, 6583 Å lines are detected for all but one source (No. 11 at $z = 0.1186$ in Fig. A1), where only the [N II] λ6583 Å line is detected. The fluxes of these lines, tabulated in the VAC, are thus reliably detected for each source, where present, in the DESI spectra, using the automated procedure outlined in H. Zou et al. (2024). This is further shown by the consistency in our determined abundances compared to I. A. Zinchenko et al. (2024) in Section 2.4. We reiterate that the spectra are shown only for visual confirmation, and the required tabulated line fluxes from the VAC are utilized for abundance determination in this work.

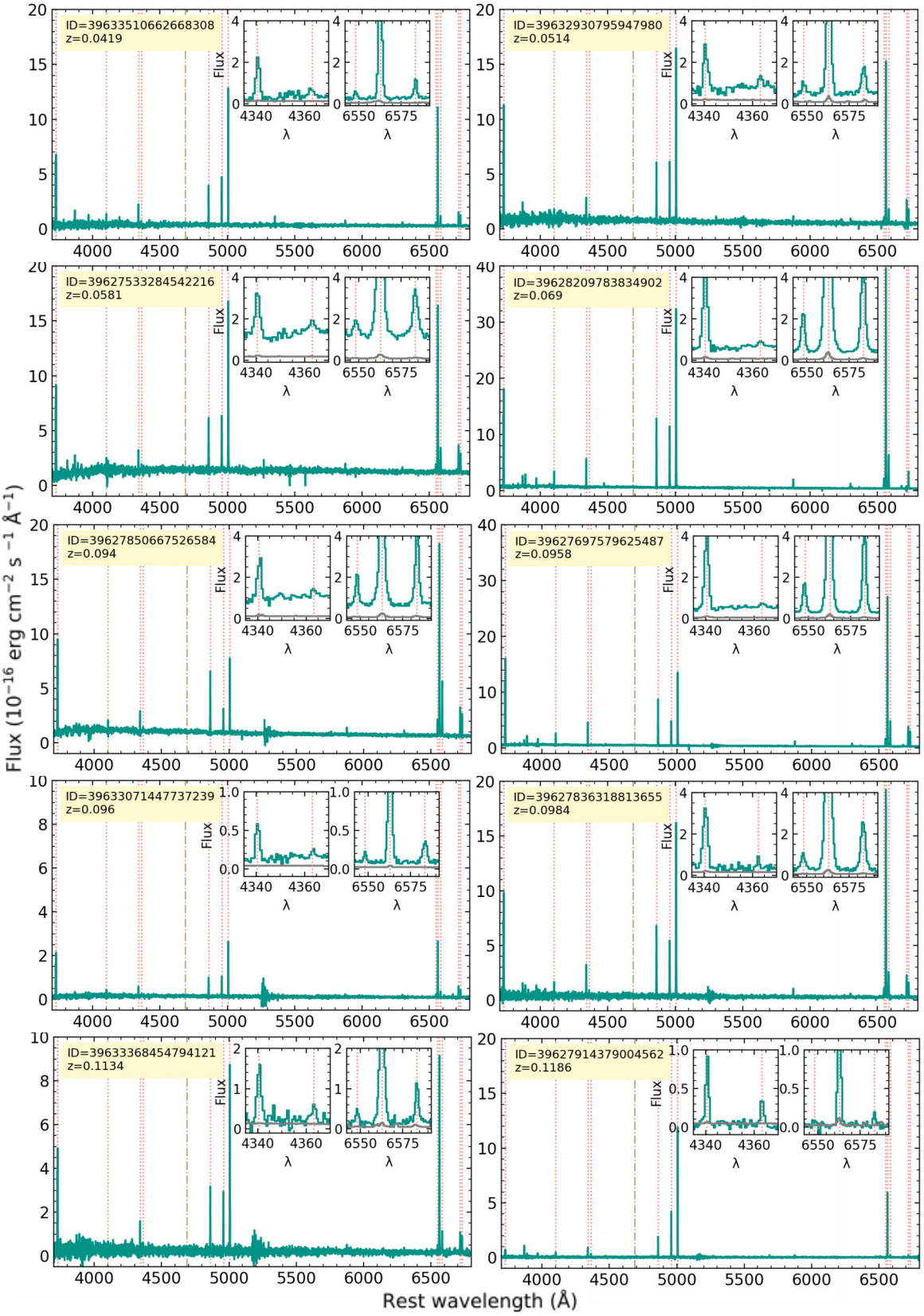

Figure A1. Same as Fig. 1, but showing the DESI spectra for the N-emitters Nos 2–11 in Table 2. The insets clearly show the detections of the [O III] λ4363 Å and [N II] λ6583 Å lines in all sources, with the [N II] λ6548 Å line also detected in all but one source. Note also that the axis scales vary for each spectrum (also for the insets) to accommodate the fluxes of the brightest lines.

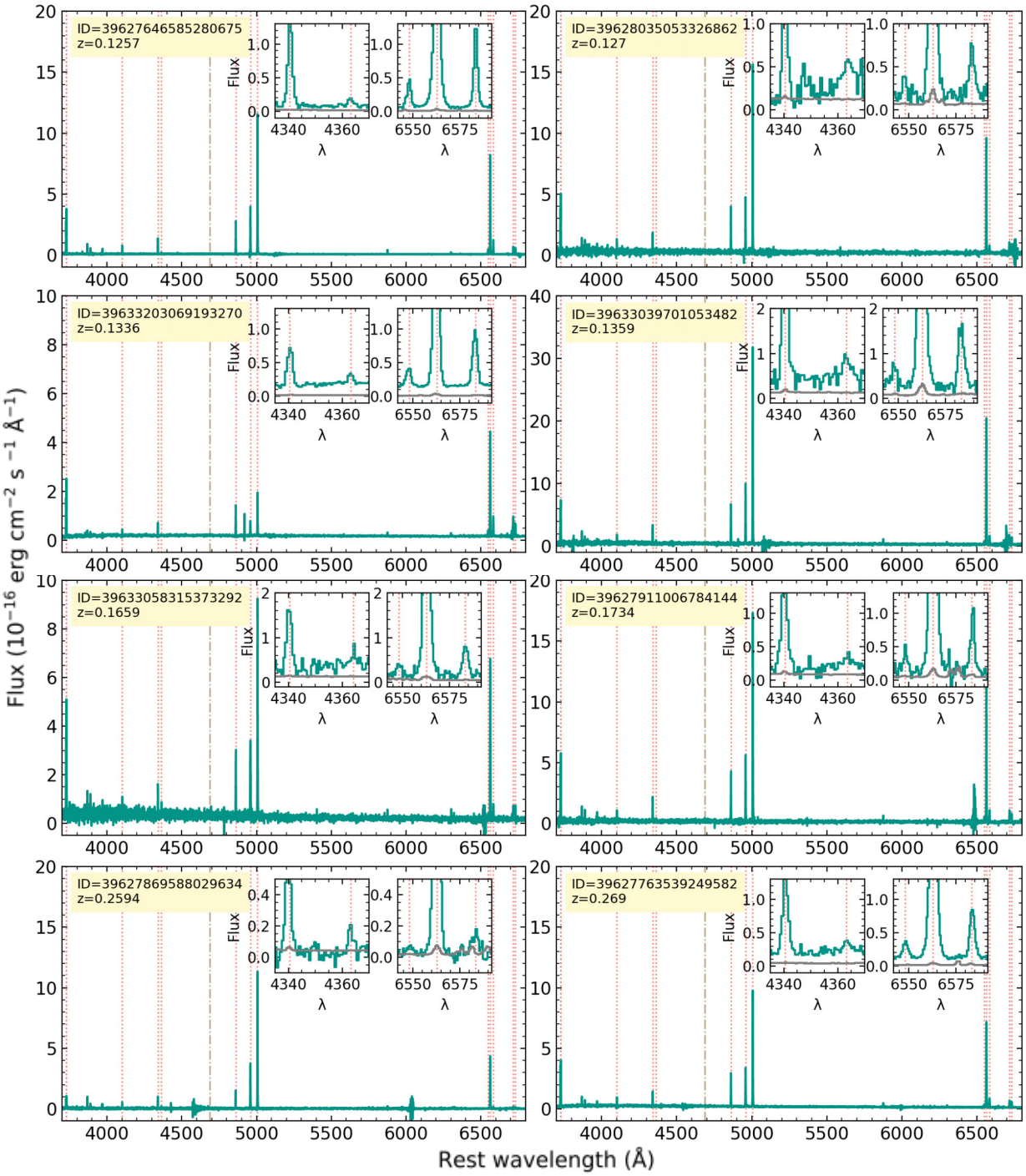

Figure A2. Same as Fig. A1, but showing the DESI spectra for the N-emitters Nos 12–19 in Table 2. The insets clearly show the detections of the [O III] λ4363 Å and [N II] λλ6548, 6583 Å lines in all sources.

APPENDIX B: STACKED SPECTRA OF EXTREME N-EMITTERS

While the He II λ4686 Å line remains undetected for any of our N-emitters (see Figs 1, A1, and A2), it does not rule out the presence of WR stars in these SFGs as this line is intrinsically faint even in confirmed WR galaxies (the flux of this line can be ∼0.0025 times that of the [O III] λ5007 Å line; A. R. López-Sánchez & C. Esteban 2009). We further computed the stacked spectrum from the individual DESI spectra of the 19 N-emitters, adopting the spectral resampling using SPECTRES (A. C. Carnall 2017) and normalized to their [O III] λ5007 Å line fluxes. Fig. B1 shows the stacked spectrum as well as the normalized spectra of the 19 N-emitters covering the wavelength range of the He II λ4686 Å and H β lines.

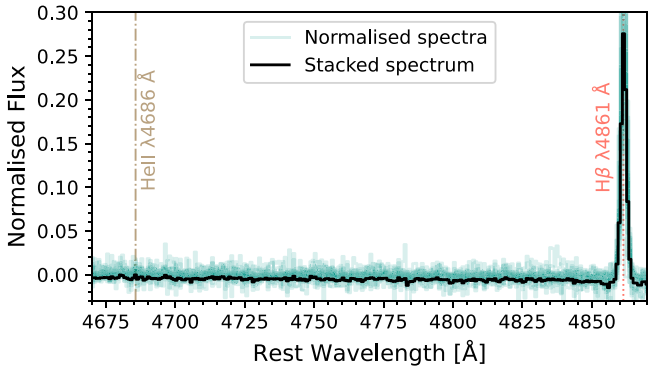

Figure B1. The stacked spectrum is shown in black, while the normalized spectra of the 19 N-emitters in Table 2 are shown in green (they overlap with each other in the noise, but the H β line is clear). The wavelength range covers the marked position of the undetected He II λ4686 Å line and the clear H β line.

It is clear that the He II λ4686 Å line is not detected in the stacked spectrum either, even though the noise in the spectrum is clearly reduced compared to the individual normalized spectra. The 3σ detection limit at the position of the He II λ4686 Å line (relative to the [O III] λ5007 Å line) is 0.018, so indeed even known WR galaxies (e.g. with this ratio being $\sim$0.0025; A. R. López-Sánchez & C. Esteban 2009) would remain undetected. Thus, we can neither confirm nor rule out the presence of WR stars even with the stacked spectra.

This paper has been typeset from a TEX/LATEX file prepared by the author.